ASME Journal of Mechanisms and Robotics
Online journal at:
https://asmedigitalcollection.asme.org/mechanismsrobotics

Development of a Base-Actuated Three-Rhombus Configured Remote Center of Motion Mechanism for Lumbar Puncture

Yuzhou Duan
College of Mechanical and Electrical Engineering,
Nanjing University of Aeronautics and Astronautics,
Nanjing 210016, China

Jie Ling[1]
College of Mechanical and Electrical Engineering,
Nanjing University of Aeronautics and Astronautics,
Nanjing 210016, China
e-mail: meejling@nuaa.edu.cn

Zhao Feng
College of Power and Mechanical Engineering,
Wuhan University,
Wuhan 430072, China

Daojin Yao
School of Electrical and Automation Engineering,
East China Jiaotong University,
Nanchang 330013, China

Yuchuan Zhu
College of Mechanical and Electrical Engineering,
Nanjing University of Aeronautics and Astronautics,
Nanjing 210016, China

Owing to the advantages of safety and reproducibility, remote center of motion (RCM) mechanisms are widely adopted in lumbar puncture (LP) procedures to guide the insertion angle and depth of the end effector. However, the proximal-actuated pattern in existing RCM mechanisms occupies a large space near the end effector, which obstructs the visual field and increases the system inertia. In this work, a base-actuated three-rhombus configured RCM mechanism for LP operation is first proposed, where the symmetric three-rhombus scheme is designed for motion transmission. As a result, the rotational and translational motions of the needle are respectively realized through the homodromous and heterodromous actuation of the two base-mounted motors. Kinematic models are established to analyze the manipulability, singularity, and workspace of the RCM mechanism theoretically. The parameter optimization procedure is provided to minimize the footprint of the RCM mechanism. Experimental results show that the mechanism reaches an insertion angle from −29.2 deg to 29.2 deg, a maximum insertion depth of 60.02 mm, and a footprint of 4.98×10^4 mm^2. The relative error of the RCM point is 1.1 mm. [DOI: 10.1115/1.4062761]

Keywords: mechanism design, medical robots, remote center of motion mechanism

1 Introduction

Lumbar puncture (LP) is a challenging medical skill, where high precision of needle insertion angle and depth is required to reduce the number of puncture attempts [1], especially in the case of narrowed interspinous or interlaminar spaces [2]. As shown in Fig. 1(*a*), during the LP procedure, a thin but hollow needle is inserted through the ligaments between lumbar vertebrae, punctures dura arachnoid mater, and finally enters spine canal to collect cerebrospinal fluid or to perform spinal anesthesia [3,4], which indicates the LP an indispensable medical procedure in modern diagnosis and treatment field. Compared with manual insertion, robotic-assisted needle insertion reveals its great advantages in insertion accuracy and reproducibility [5–7].

A remote center of motion (RCM) mechanism is a key mechanical component in a needle insertion robot to ensure that the needle is within the insertion point with its special mechanical structure [8,9]. Therefore, the risk of robot-patient collisions is physically reduced [10]. As shown in Fig. 1(*b*), due to the constraints of the insertion point, the needle has up to four degrees-of-freedom (DOF), including three rotational and one translational (3R1T, R: rotational, T: translational) motions. In LP, the rotation along the needle axis is not required. Therefore, the RCM mechanisms for LP require only 2R1T motions.

To synthesize a 2R1T RCM mechanism, a widely used method is to combine a 1R1T RCM mechanism and a 1R mechanism in series with their RCM points coincided [11]. A lot of efforts have been carried out on 1R RCM mechanisms [12–14], and some have been applied in commercial applications (e.g., the da Vinci surgery system [15]). To broaden applications based on 1R RCM mechanisms, some 1R1T planar RCM mechanisms have been put forward for specific surgery applications, such as dual trigonometric-ratio-based structure for compact bone surgery [16], scissor-linkage-based structure for breast ultrasound scanning [17], and structure including dual-triangular and straight-line linkages for minimally invasive surgeries [18]. In addition, type synthesis has been conducted for the innovative design of RCM mechanisms. A synthesis method of closed-loop 1R1T RCM mechanisms was proposed inspired by pantograph mechanisms [11]. According to the concept of a virtual center of motion, a new family of RCM mechanisms is synthesized [19]. Based on virtual parallelograms, a class of 2DOF planar RCM mechanisms was proposed [20]. Among the existing RCM mechanisms, the proximal-actuated pattern is the most common and simplest actuation pattern, realizing the translation motion of the end effector by installing linear motors near the end. Nevertheless, this type of actuation pattern occupies much space near the end effector, which increases the collision risk and the system inertia.

To this end, some base-actuated RCM mechanisms have been proposed. Cable-driven methods are adopted to achieve base actuation. Based on closed-loop cable transmissions, a class of planar 2DOF RCM mechanisms without active or passive translational joints are proposed in Ref. [21]. In Ref. [22], a novel cable-driven RCM mechanism was proposed to improve the footprint, i.e., the area enclosed by the outer boundary. In addition, linkage

[1]Corresponding author.

Manuscript received August 18, 2022; final manuscript received June 12, 2023; published online July 20, 2023. Assoc. Editor: Reza Fotouhi.

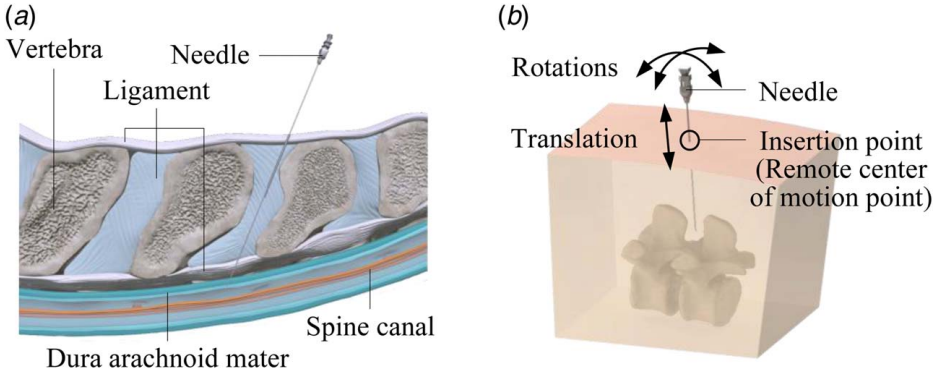

Fig. 1 Schematics of the needle insertion into lumbar vertebrae: (*a*) the anatomy of lumbar punctures and (*b*) the required degrees-of-freedom in lumbar punctures

transmission can also achieve base actuation through reasonable structure design. By connecting two sets of parallel links, a base-actuated RCM mechanism with good mechanical properties was developed in Ref. [23]. A novel parallelogram-based RCM mechanism was proposed in Ref. [24] with its linear motor distally. In conclusion, (a) the current base-actuation configurations are limited, (b) cable-driven method is relatively more compact than the linkage transmission method; however, the transmission error of the cable-driven method is larger than linkage structures. Therefore, linkage transmission is adopted in this paper to meet the accuracy requirement in LP. Compactness is also included as a design goal under the premise that the insertion requirements can be reached.

The motivation of this work is to develop a novel base-actuated 1R1T RCM mechanism with a compact structure that satisfies the requirements of LP operation, ensuring adequate accuracy and workspace. The core idea is that the rotational and translational motions of the end effector can be decoupled and realized respectively through the homodromous and heterodromous actuation of the two base-mounted motors. Furthermore, a 2R1T mechanism can be simply obtained by applying a rotation part to the proposed mechanism. The main novelty lies in (a) the base-actuated pattern realized by this RCM mechanism through the three-rhombus transmission scheme, (b) the rotational and translational motions of the needle that fit the LP requirements are decoupled by the selected actuation method, (c) compared with Refs. [23–25], this mechanism implements the base-actuated pattern with a more compact footprint. The contributions of this paper can be summarized as (a) proposing a novel base-actuated three-rhombus transmission scheme for RCM mechanisms' development, (b) providing a modeling and parameter optimization procedure to minimize the footprint of the RCM mechanism, and (c) presenting the physical test scheme for intuitional evaluations of the proposed RCM mechanism.

The remainder of this paper includes the following parts. Section 2 conducts the preliminary design including the analysis of LP and the type synthesis work. Kinematic models and the performance indices are depicted in Sec. 3. In Sec. 4, parameter optimization is performed to minimize the footprint. In Sec. 5, a prototype is presented. The footprint, accuracy, repeatability, and workspace of the prototype are measured and discussed. The concluding remarks are given in Sec. 6.

2 Preliminary Design

This section presents the preliminary design of the proposed three-rhombus RCM mechanism. LP procedure is analyzed first from the perspective of engineering. Then, the three-rhombus structure is obtained by type synthesis.

2.1 Lumbar Puncture Analysis. The required insertion angle, depth, and accuracy are analyzed in this part. In LP, there are two common insertion approaches: the midline approach and the paramedian approach. As shown in Fig. 2(*a*), for the midline approach, the needle axis is located in the median plane, and the angle between the needle axis and sagittal axis is 10 deg. As shown in Fig. 2(*b*), for the paramedian approach, the angle between the needle axis and the median plane is 15 deg, and the angle between the projection of the needle and the sagittal axis is about 15 deg [26]. As a result, the insertion angle, i.e., twice the angle between the needle axis and the sagittal axis, needs to be designed larger than 42.2 deg. According to Ref. [27], the mean distance from the skin to the subarachnoid space is about 51.3 ± 6.9 mm. Considering a clearance between the needle tip and the insertion point, the insertion depth is determined as 60 mm. Epidural space is the narrowest part the needle needs to pass through, of which the maximum width is 5–6 mm [26]. Therefore, the maximum accuracy of the RCM point should reach half width of the epidural space (i.e., less than 2.5 mm).

2.2 Type Synthesis. On the basis of the variations of the rhombic structure, a planar three-rhombus configured RCM mechanism with 2DOF is proposed, enabling base actuation, a 2R1T mechanism can be simply obtained by applying a rotation mechanism at the base. The schematic of the proposed structure is presented in Fig. 3(*a*). The proposed RCM mechanism consists of two active linkages in purple, two middle rhombic mechanisms in blue, one end rhombic mechanism in green, and one end effector in yellow. Actuated by the active linkages and assisted by the middle rhombic mechanisms, the trajectory of point A_i' ($i = 1, 2$) moves along the mirror trajectory of point A_i with respect to the $M_{11}M_{22}$ axis; therefore, the motions of points A_1' and A_2' are on the arc centered on O'. Then, assisted by the end rhombic mechanism, the end effector EF processes 1R1T motions.

Figure 3(*b*) presents one of the middle rhombic mechanisms in Fig. 3(*a*). Constrained by the kinematic pairs, the motion of point A_1' is the mirror motion of point A_1 according to symmetry. In the proposed RCM mechanism, the motion of point A_1' is an arc. As

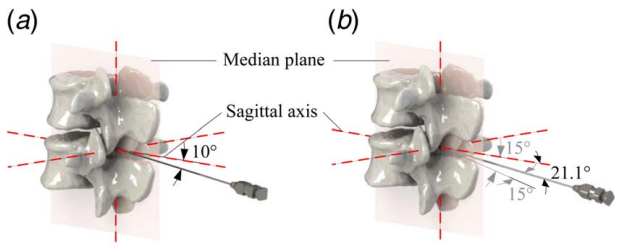

Fig. 2 Diagram illustrating paramedian and midline approaches of lumbar punctures: (*a*) the midline approach and (*b*) the paramedian approach

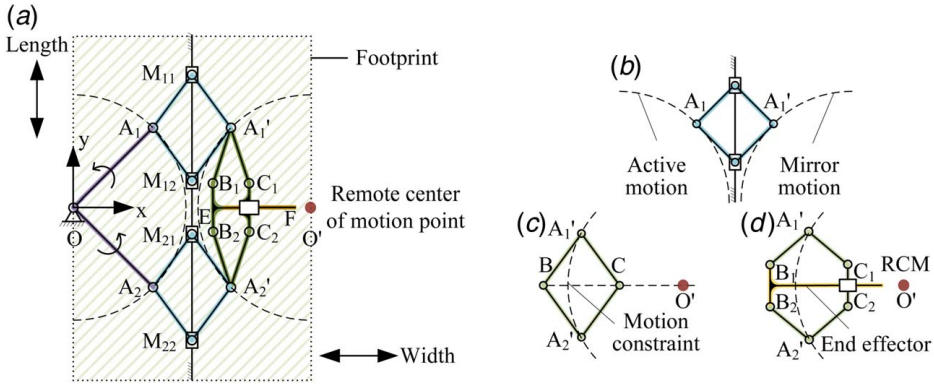

Fig. 3 Schematics and type synthesis of the three-rhombus remote center of motion mechanism: (*a*) the overall structure, (*b*) the middle rhombic mechanism, (*c*) the origin end rhombic mechanism, and (*d*) the variation of the end rhombic mechanism (Color version online.)

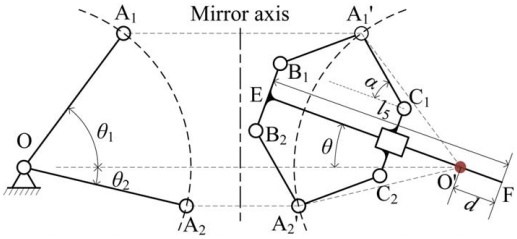

Fig. 4 Kinematic structure of the three-rhombus remote center of motion mechanism

shown in Fig. 3(*c*), the motions of point A_1' and point A_2' are constrained in the same arc so that line BC always crosses O′. Based on this, the variation of the mechanism in Fig. 3(*c*) is presented in Fig. 3(*d*), where an end effector is introduced in the middle of the rhombic mechanism. In that way, the end effector has an RCM (point O′). When two points A_1' and A_2' are constrained to the arc moving around the arc in the same direction with the same speed (homodromous actuation), the end effector has a rotation motion around the RCM; when the points rotate in the opposite direction with the same speed (heterodromous actuation), the end effector has a translation motion along the end effector.

3 Kinematic Modeling and Analysis

This section derives both the forward and inverse kinematics of the three-rhombus RCM mechanism, further deducing the Jacobian matrix. Then, the performance indices of the mechanism including the manipulability, singularity, and workspace are derived and analyzed.

3.1 Forward Kinematics. The simplified kinematic structure of the mechanism is presented in Fig. 4. The middle rhombic mechanisms are omitted and replaced by a mirror axis that indicates the mirror motion of points A_1 and A_2 with respect to the points A_1' and A_2'. OA_1 and OA_2 are the two active linkages, θ_1 and θ_2 are the input variables of the mechanism, θ is the insertion angle, and d is the insertion depth. The length of each linkage is defined in Table 1.

The outputs of the mechanism are typically denoted by the insertion angle and depth of the end effector. In Fig. 4, actuated by linkages OA_1 and OA_2 respectively, the insertion angles of the end effector can be directly obtained by the geometrical relationship, which can be expressed as follows:

$$\theta = \frac{1}{2}(\vartheta_1 + \theta_2) \tag{1}$$

where counterclockwise is positive for θ_1 and θ_2.

By solving a simple geometry problem, the insertion depth of the end effector can be represented as follows:

$$d = l_5 - l_3\cos\,\alpha - l_1\cos\left(\frac{\theta_1 - \theta_2}{2}\right) \tag{2}$$

where d represents the displacement between point O′ and F. α represents the acute angle between lines $A_1'C_1$ and B_1C_1, which has the following expression:

$$\alpha = \arcsin\left(\frac{1}{l_3}\left(l_1\sin\left(\frac{\theta_1 - \theta_2}{2}\right) - \frac{l_4}{2}\right)\right) \tag{3}$$

3.2 Inverse Kinematics. By performing simple mathematical operations on Eqs. (1) and (2), the inverse kinematics can be written as follows:

$$\begin{cases} \theta_1 = \theta + \Delta \\ \theta_2 = \theta - \Delta \end{cases} \tag{4}$$

with

$$\begin{cases} d_0 = l_5 - d \\ c = d_0^2 + l_1^2 - l_3^2 + \dfrac{l_4^2}{4} \\ \Delta = \arccos\left(\dfrac{c}{l_1\sqrt{4d_0^2 + l_4^2}}\right) + \arctan\left(\dfrac{l_4}{2d_0}\right) \end{cases} \tag{5}$$

where d_0, c, and Δ are intermediate variables with respect to d, generated by geometric operations. From Eqs. (4) and (5), it can be

Table 1 Linkage parameters of the three-rhombus remote center of motion mechanism

Linkage	OA_1, OA_2	A_iM_{ij}, $A_i'M_{ij}$ $(i=1,2;j=1,2)$	$A_1'B_1$, $A_2'B_2$, $A_1'C_1$, $A_2'C_2$	B_1B_2, C_1C_2	EF
Parameter	l_1	l_2	l_3	l_4	l_5

Table 2 Values of the RCM mechanism parameters after optimization

Parameter	l_1	l_2	l_3	l_4	l_5	l_s	θ_s	α_1	α_2
Value	63 mm	66 mm	52 mm	8 mm	107.13 mm	60.02 mm	58.41 deg	21.32 deg	78.69 deg

concluded that the output θ and d can be decoupled by the inputs $(\theta_1+\theta_2)/2$ and $(\theta_1-\theta_2)/2$, i.e., when linkages OA_1 and OA_2 rotate in the same direction with the same speed, the end effector has a pure rotation motion; when the two linkages rotate in the opposite direction with the same speed, the end effector has a pure translation motion.

3.3 Jacobian Matrix. To derive the Jacobian matrix, vector forms of both input and output variables are proposed. The relationship between the input vector $\boldsymbol{x}$ and output vector $\boldsymbol{\theta}$ is defined by the following equation:

$$\boldsymbol{F}(\boldsymbol{x}, \boldsymbol{\theta}) = 0 \tag{6}$$

where $\boldsymbol{x} = [\theta, d]'$, $\boldsymbol{\theta} = [\theta_1, \theta_2]'$, and $\boldsymbol{F}$ is the implicit function that denotes the relationship between $\boldsymbol{x}$ and $\boldsymbol{\theta}$.

Differentiating function $\boldsymbol{F}$ in Eq. (6) with respect to time leads to the following equation:

$$\mathbf{A}\dot{\boldsymbol{x}} + \mathbf{B}\dot{\boldsymbol{\theta}} = 0 \tag{7}$$

with

$$\mathbf{A} = \frac{\partial \boldsymbol{F}}{\partial \boldsymbol{x}}, \mathbf{B} = \frac{\partial \boldsymbol{F}}{\partial \boldsymbol{\theta}} \tag{8}$$

where $\mathbf{A}$ and $\mathbf{B}$ are both the Jacobian matrices.

Based on the kinematic results, the substitution of Eqs. (1), (2), and (3) into Eq. (8) gives the following equation:

$$\mathbf{A} = \begin{bmatrix} -2 & 0 \\ 0 & -2 \end{bmatrix}, \mathbf{B} = \begin{bmatrix} 1 & 1 \\ \lambda & -\lambda \end{bmatrix} \tag{9}$$

with

$$\lambda = l_1 \sin\left(\frac{\theta_1-\theta_2}{2}\right) + l_1 \cos\left(\frac{\theta_1-\theta_2}{2}\right)\tan\alpha \tag{10}$$

3.4 Manipulability Analysis. Manipulability reflects the dexterity of robots, which takes the following form:

$$w = \sqrt{\det(\boldsymbol{J}\boldsymbol{J}^{\mathrm{T}})} \tag{11}$$

where $\boldsymbol{J} = -\mathbf{A}^{-1}\mathbf{B}$ is another form of the Jacobian matrix. Substitution of Eqs. (9) and (10) into Eq. (11) gives the following equation:

$$w = \frac{1}{2}\left(\tan\alpha\sqrt{l_1^2 - \left(\frac{l_4}{2} + l_3\sin\alpha\right)^2} + l_3\sin\alpha + \frac{l_4}{2}\right) \tag{12}$$

Equation (12) indicates that when α goes to zero, $\sin\alpha$ goes to zero, and $\tan\alpha$ goes to infinitely great. As a result, the manipulability goes infinitely great.

3.5 Singularity Analysis. Singularity occurs when the Jacobian matrices $\mathbf{A}$ or $\mathbf{B}$ becomes singular. In this mechanism, the singularity occurs only when

$$det(\mathbf{B}) = 0 \tag{13}$$

Substitution of Eqs. (9) and (10) into Eq. (13) gives

$$\sin\left(\frac{\theta_1-\theta_2}{2}\right) = \frac{l_4}{2(l_1-l_3)} = \sin\alpha \tag{14}$$

Let $\alpha_1 = (\theta_1-\theta_2)/2$, the singularity condition can be derived when $\alpha = \alpha_1$.

3.6 Workspace Analysis. Equation (12) demonstrates that when α goes to zero, the manipulability w goes to infinitely great; Eq. (14) denotes that when α goes to α_1, the mechanism becomes singularity. Therefore, the acute angle α satisfies the following inequations:

$$\alpha \geq \alpha_1, \alpha \leq \alpha_2 \tag{15}$$

where α_2 ($\alpha_2 \leq 90$ deg) is determined by the required kinematic property.

As has been noted, the 2DOF of the end effector, denoted by insertion depth d and angle θ, are decoupled. So the enclosed shape of the workspace is a sector, which can be easily represented as follows:

$$\begin{aligned} l_s &= \kappa_1 - \kappa_2 \\ \theta_s &= \pi - 2\arcsin\left(\frac{l_3\sin\alpha_2 + (l_4/2)}{l_1}\right) \end{aligned} \tag{16}$$

where l_s and θ_s are the radius and the arc angle of the sector respectively. The parameters κ_i ($i = 1, 2$) take the following form:

$$\kappa_i = \sqrt{l_1^2 - \left(l_3\sin\alpha_i + \frac{l_4}{2}\right)^2} - l_3\sin\alpha_i \tag{17}$$

4 Parameter Optimization and Simulations

Reduction of the footprint is well needed to avoid robot-patient collisions as well as to save limited surgical space. Therefore, the optimization objective is to minimize the footprint of the proposed mechanism. In this section, the optimization objective is stated first including the decision variables, objective function, and constraints. Then, optimization work is performed to minimize the footprint of the RCM mechanism.

4.1 Optimization Objective. The footprint of a mechanism refers to the area occupied by the mechanism at any instant of time, covering all its configurations. As shown in Fig. 3(*a*), as far as the proposed mechanism is concerned, the footprint can be

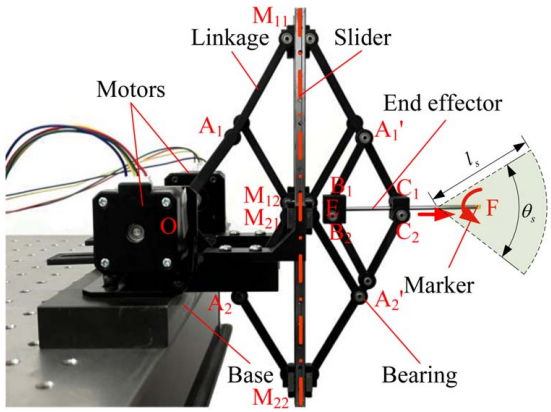

Fig. 5 Prototype of the proposed three-rhombus remote center of motion mechanism

simply defined by multiplying the maximum length and width of the mechanism (the rectangle with green stripes). The maximum length depends on the limit position of points M_{11} and M_{22}. The Cartesian coordinate system with origin O is established in Fig. 3(*a*), so the *y*-coordinate of point M_{11} takes the form

$$y_{M_{11}} = l_1 \sin\theta_1 + \sqrt{l_2^2 - l_1^2(1-\cos\theta_1)^2} \tag{18}$$

where $-\pi/2 \le \theta_1 \le \pi/2$. To ensure that the RCM mechanism can reach all the configurations of the workspace, one has $l_2 \ge l_1$. Therefore, the maximum length of the proposed mechanism f_l can be simplified as follows:

$$f_l(l_1) = 2\max\left(y_{M_{11}}(\theta_1)\big|_{l_2=l_1}\right) = 2\sqrt{2}l_1 \tag{19}$$

The maximum width is the distance between the points O and O′, which is $2l_1$. Then, the footprint can be represented as follows:

$$f_s(l_1) = 4\sqrt{2}l_1^2 \tag{20}$$

where f_s, which stands for the footprint of the mechanism, is the optimization objective.

According to the workspace requirements of LP, the constraints can be derived. The radius l_s and the arc angle θ_s of the workspace sector need to satisfy the following inequations:

$$l_s(l_1, l_3) \ge l_r,\ \theta_s(l_1, l_3) \ge \theta_r \tag{21}$$

where l_r and θ_r are the required length and angle of the sector-shaped workspace. In this paper, as analyzed in Sec. 2, one has $l_r = 60$ mm, $\theta_r = 42.2$ deg.

Equations (20) and (21) illustrate that l_1 and l_3 are two independent decision variables. With all the analyses above, the optimization problem can be concluded in mathematical terms

$$\begin{gathered}\text{Objective function}: \min f_s(l_1) = 4\sqrt{2}l_1^2 \\ \text{Independent variables}: l_1 \text{ and } l_3 \\ \text{s.t.} \begin{cases} {}_s(l_1, l_3) \ge 60\,\text{mm} \\ \theta_s(l_1, l_3) \ge 42.2\,\text{deg} \end{cases}\end{gathered} \tag{22}$$

4.2 Optimal Design. MATLAB Optimization Toolbox is adopted to perform the optimization work. The initial values of the independent variables that satisfy the constraints are randomly chosen as $[l_1,\ l_3] = [150,\ 80]$. And the optimization result is $[l_1,\ l_3] = [62.96,\ 51.6]$.

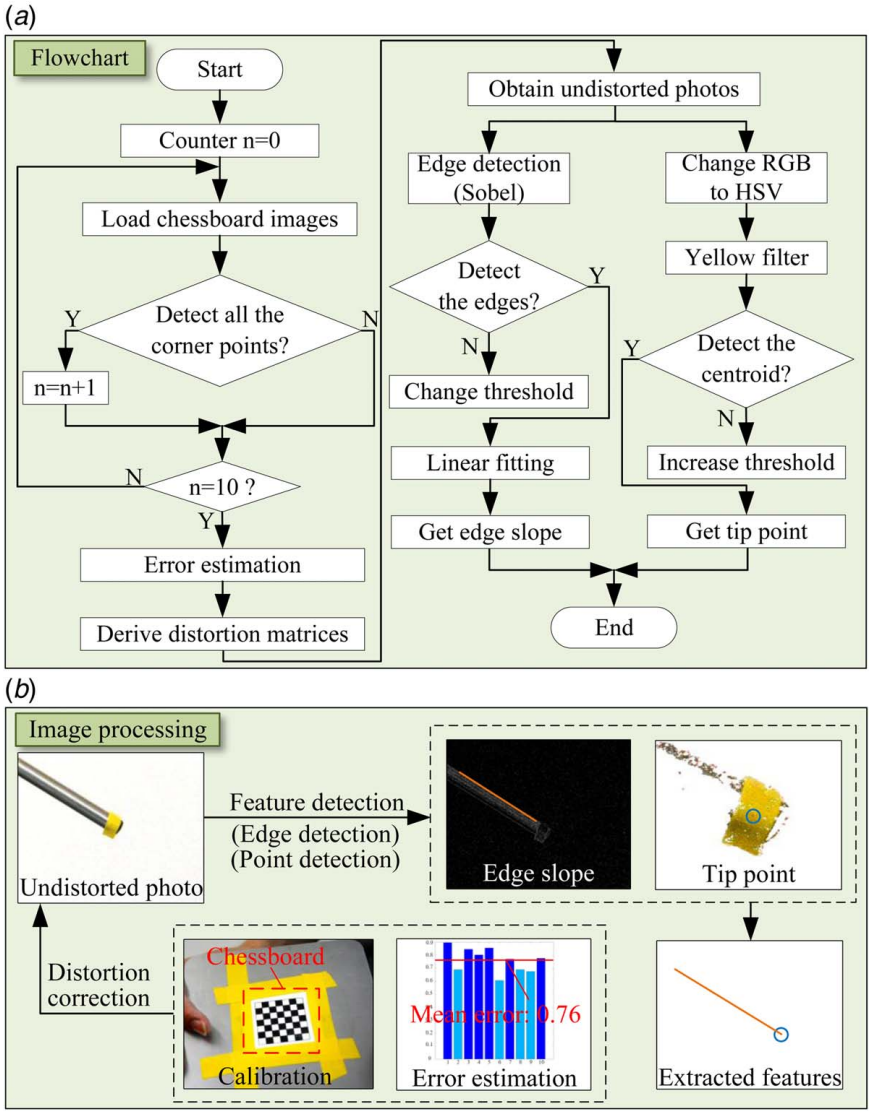

Fig. 6 Image processing of the camera photos: (*a*) the flowchart of the image processing and (*b*) the specific procedure of image processing

It is worth mentioning that after optimization the arc angle θ_s doesn't reach the limit (58.4 deg versus 42.2 deg), which results in a larger insertion angle of the needle. To ensure the installation space in the subsequent prototype, there is a 3 mm increase in l_2 (66 mm). The length of l_4 is 8 mm for the further installation of the end effector and rotational pairs. The length of l_5 is derived from Eq. (2) to ensure the tip of the end effector reaches the RCM point when $d=0$. Table 2 lists all the parameters of the mechanism.

5 Experimental Characterization

The experimental characterization of the optimized mechanism including the measurements of the footprint, RCM point, repeatability, and workspace are conducted in this section based on a prototype.

5.1 Experimental Setup. A physical prototype was fabricated in Fig. 5 to intuitively validate the effectiveness of the proposed three-rhombus RCM mechanism. All the linkages of the prototype are made of resin and 3D printed with the accuracy of 200 μm (type 8000, Wenext Inc., Shenzhen, China) and connected by flange bearings. Two motors are used to actuate the active linkages, the sliders are adopted to produce sliding motion, and the linear bearing is used to act as column pair (SAMLO Inc., Shenzhen, China). The motion signals of the motors are generated by the data acquisition board PCI-6259 (National Instruments Co., Austin, TX, USA). The position of the end effector is recorded by a monocular camera (Nikon D5200).

The image-based method is employed to obtain the configuration of the end effector. The flowchart of the image processing is illustrated in Fig. 6(*a*), and the specific procedure is shown in Fig. 6(*b*). First, the camera is calibrated by the chessboard with 10 chessboard images; then, distortion matrices are derived to perform distortion correction on the original photos of the end effector (distortion correction). The mean error of the calibration is 0.76 pixels. After processing, the edge slope and tip point, which are the required features of the end effector, are extracted from undistorted photos (feature detection). The camera has 24×10^6 effective pixels, the focal length of the lens is 18 mm, and the distance of the end effector is set at 38.67 mm (derived from calibration).

5.2 Compactness Validation With Workspace-Footprint-Ratio Index. We define an index named workspace-footprint-ratio (WFR) to quantitatively describe the compactness of RCM mechanisms. The WFR is the ratio of workspace to footprint for a mechanism, due to the positive correlation between workspace and footprint. Therefore, the dimensionless WFR index can be used to describe compactness. The footprint of our mechanism can be directly measured through the undistorted camera photos, which is 4.98×10^4 mm^2. Compared with the theoretical value of 3.56×10^4 mm^2, the growth is mainly due to the additional volume of linkages and moving pairs. As shown in Table 3, our paper achieves the largest WFR index (38%), which means the most compact. (for spatial RCM mechanisms, only planar workspaces are computed).

Table 3 Comparison of the WFR index of our RCM mechanism with other recent RCM mechanisms

Reference	Workspace	Footprint	WFR index
[23]	1.4×10^4	$>4.2\times10^5$	<3.3%
[24]	1.8×10^4	$>5.7\times10^4$	<31%
This paper	3.3×10^4	5.0×10^4	**38%**
[25]	5.8×10^1	3.5×10^3	1.7%

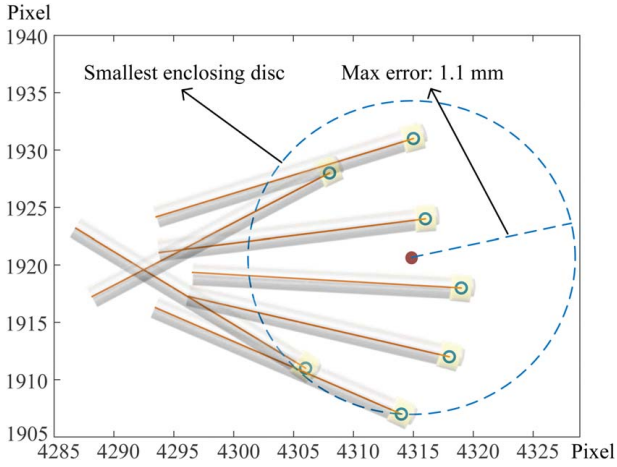

Fig. 7 Accuracy measurement of the remote center of motion point

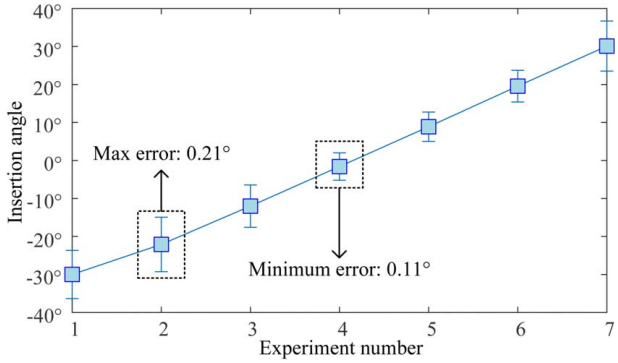

Fig. 8 Error band plot for insertion angle repeatability test

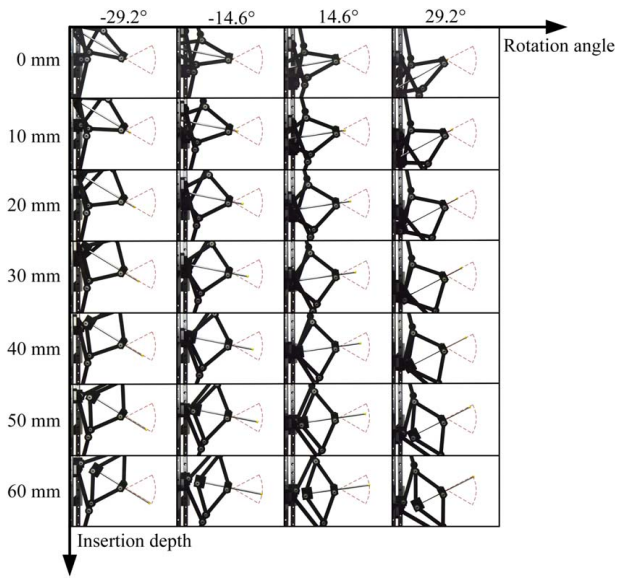

Fig. 9 Workspace validation of the proposed mechanism based on the prototype

5.3 Accuracy Measurement of the Remote Center of Motion Point. The kinematics of the mechanism ensures that the tip of the end effector coincides with the nominal RCM point when the insertion depth satisfies $d=0$. However, in practice, small deviation occurs due to some inevitable factors such as machining error, assembly error, and the slight deflection of the linkages. The

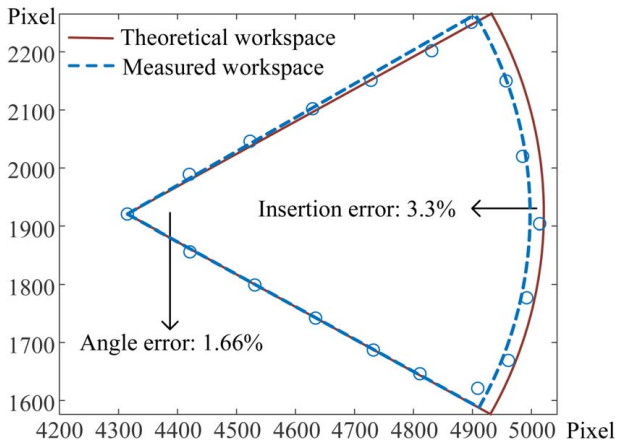

Fig. 10 Accuracy measurement of the workspace: insertion angle and depth

accuracy of the RCM point is the key to decreasing the number of puncture attempts in the LP. Therefore, the accuracy characterization of the practical RCM point was conducted by photoing seven different insertion angles evenly in the workspace when $d = 0$; $\theta = 29.2\,\text{deg}, 19.5\,\text{deg}, 9.7\,\text{deg}, 0\,\text{deg}, -9.7\,\text{deg}, -19.5\,\text{deg}, -29.2\,\text{deg}$. The result is shown in Fig. 7, where the nominal RCM point is selected by the smallest enclosing disc approach. The relative accuracy of the RCM point is 1.1 mm. Also, the theoretical RCM point (relative to the base) is calculated according to the calibrated images. The pixel coordinate of the theoretical RCM point is $(x, y) = (4310.6, 1953.3)$. Then, the absolute accuracy of the RCM point is derived at 2.97 mm. We notice that the error mainly comes from the y-axis, which is 2.94 mm. After image analysis, we believe that the main reason lies in the assembly error of the sliders, which leads to an overall y-axis offset.

5.4 Repeatability Test of the Insertion Angle. In this part, the repeatability of the insertion angles is tested. The accuracy of the RCM point which has been tested determines the accuracy of the needle tip distance from the ideal insertion point. The repeatability of the insertion angles determines the orientation accuracy. Seven insertion angles are chosen evenly from $-29.2\,\text{deg}$ to $29.2\,\text{deg}$ and for each insertion angle, the experiment is repeated five times. Then, we made error band plots to evaluate the repeatability of the insertion angles, as shown in Fig. 8. The index of the error bar is the standard error, which is magnified 15 times for better illustration. Results show that the maximum standard error is $0.21\,\text{deg}$, demonstrating the good repeatability of the insertion angle.

5.5 Validation and Accuracy Measurement of the Workspace. Workspace characterization was conducted on the prototype by evenly photoing 49 configurations in its workspace, as shown in Fig. 9. The results demonstrate that the prototype reaches the insertion angle ranging from $-29.2\,\text{deg}$ to $29.2\,\text{deg}$ and the insertion depth ranging from 0 mm to 60.02 mm, which satisfies the workspace requirement of the LP. Compared With the narrowest part of the LP procedures (epidural space, 5–6 mm), the maximum error is also acceptable.

Workspace measurement was also conducted for further verification. Nineteen configurations from the periphery in Fig. 9 were chosen to estimate the accuracy of the workspace. As shown in Fig. 10, the tip points of the 19 configurations form the outer contour of the workspace. By using linear fitting technique, the position of the two sides of the sector was obtained; the radius of the sector was obtained by taking the average of the displacements between the related points and the nominal RCM point. Results show that the error of the prototype reaches 1.66% at the arc angle and 3.3% at the radius. During the experiment, we noticed the defects of relatively low stiffness and high dampness in our prototype, which was embodied by the slight displacement decay during multiple needle insertion (3.3%). In addition, a slight feed motion of the end effector would happen when a small external disturbance was applied after each insertion motion.

6 Conclusion

This paper presents the design and validation of a base-actuated three-rhombus configured RCM mechanism with 1R1T for LP. The required workspace and accuracy of the LP are analyzed first. Then, a novel three-rhombus structure of the proposed mechanism is synthesized in conceptual design to realize the base-actuated pattern. Kinematics of the mechanism are derived and performance indices are deduced for further optimization work. The optimization is carried out to form a specific-sized mechanism with the objective of minimizing the footprint of the mechanism. A prototype based on the optimized parameters is presented and verifies the effectiveness of the proposed mechanism. The test results show that the relative accuracy and workspace of the prototype can meet the requirements of LP. In addition, the prototype processes a compact structure and good repeatability.

Due to the inherent defects of multi-linkage drive systems, our further research will devote to establishing new transmission schemes and control methods to further increase the accuracy of the RCM point.

Acknowledgment

This work is funded by the Fundamental Research Funds for the Central Universities (Grant No. NS2022051), Natural Science Foundation of Jiangsu Province (Grant No. BK20210294), and Key Research Development Plan of Jiangxi Province (Grant No. 20212BBE51010).

Conflict of Interest

There are no conflicts of interest.

Data Availability Statement

No data, models, or code were generated or used for this paper.

Abbreviations

R = rotation
T = translation
LP = lumbar puncture
DOF = degrees-of-freedom
RCM = remote center of motion
3D = three-dimensional

References

[1] Engelborghs, S., Niemantsverdriet, E., Struyfs, H., Blennow, K., Brouns, R., Comabella, M., Dujmovic, I., *et al.*, 2017, "Consensus Guidelines for Lumbar Puncture in Patients With Neurological Diseases," Alzheimer's Dementia: Diagn., Assess. Dis. Monit., **8**, pp. 111–126.
[2] Rizk, M. S., Zeeni, C. A., Bouez, J. N., Bteich, N. J., Sayyid, S. K., Alfahel, W. S., and Siddik-Sayyid, S. M., 2019, "Preprocedural Ultrasound Versus Landmark Techniques for Spinal Anesthesia Performed by Novice Residents in Elderly: A Randomized Controlled Trial," BMC Anesthesiol., **19**(1), p. 208.
[3] Ambastha, S., Umesh, S., Dabir, S., and Asokan, S., 2018, "Comparison of Force Required for Lumbar Puncture With Different Gauges of Spinal Needle Using Fiber Bragg Grating Force Device," IEEE Sens. J., **18**(19), pp. 8028–8033.
[4] Bolea, J., Lázaro, J., Gil, E., Rovira, E., Remartínez, J. M., Laguna, P., Pueyo, E., Navarro, A., and Bailón, R., 2017, "Pulse Rate and Transit Time Analysis to Predict Hypotension Events After Spinal Anesthesia During Programmed Cesarean Labor," Ann. Biomed. Eng., **45**(9), pp. 2253–2263.

[5] Khadem, M., Rossa, C., Usmani, N., Sloboda, R. S., and Tavakoli, M., 2016, "A Two-Body Rigid/Flexible Model of Needle Steering Dynamics in Soft Tissue," IEEE/ASME Trans. Mechatron., **21**(5), pp. 2352–2364.
[6] Adagolodjo, Y., Goffin, L., De Mathelin, M., and Courtecuisse, H., 2019, "Robotic Insertion of Flexible Needle in Deformable Structures Using Inverse Finite-Element Simulation," IEEE Trans. Rob., **35**(3), pp. 697–708.
[7] Garg, B., Mehta, N., and Malhotra, R., 2020, "Robotic Spine Surgery: Ushering in a New Era," J. Clin. Orthop. Trauma, **11**(5), pp. 753–760.
[8] Chen, G., Wang, J., Wang, H., Chen, C., Parenti-Castelli, V., and Angeles, J., 2020, "Design and Validation of a Spatial Two-Limb 3R1T Parallel Manipulator With Remote Center-of-Motion," Mech. Mach. Theory, **149**, p. 103807.
[9] Kim, C.-K., Chung, D. G., Hwang, M., Cheon, B., Kim, H., Kim, J., and Kwon, D.-S., 2019, "Three-Degrees-of-Freedom Passive Gravity Compensation Mechanism Applicable to Robotic Arm With Remote Center of Motion for Minimally Invasive Surgery," IEEE Rob. Autom. Lett., **4**(4), pp. 3473–3480.
[10] Cui, Z., Li, W., Zhang, X., Chiu, P. W. Y., and Li, Z., 2021, "Accelerated Dual Neural Network Controller for Visual Servoing of Flexible Endoscopic Robot With Tracking Error, Joint Motion, and RCM Constraints," IEEE Trans. Ind. Electron., **69**(9), pp. 9246–9257.
[11] Long, H., Yang, Y., Jingjing, X., and Peng, S., 2016, "Type Synthesis of 1R1T Remote Center of Motion Mechanisms Based on Pantograph Mechanisms," ASME J. Mech. Des., **138**(1), p. 014501.
[12] Wilson, J. T., Gerber, M. J., Prince, S. W., Chen, C.-W., Schwartz, S. D., Hubschman, J.-P., and Tsao, T.-C., 2018, "Intraocular Robotic Interventional Surgical System (IRISS): Mechanical Design, Evaluation, and Master-Slave Manipulation," Int. J. Med. Rob. Comput. Assist. Surg., **14**(1), p. e1842.
[13] Wang, Z., Zhang, W., and Ding, X., 2020, "Design and Analysis of a Novel Mechanism With a Two-DOF Remote Centre of Motion," Mech. Mach. Theory, **153**, p. 103990.
[14] Essomba, T., and Vu, L. N., 2018, "Kinematic Analysis of a New Five-Bar Spherical Decoupled Mechanism With Two-Degrees of Freedom Remote Center of Motion," Mech. Mach. Theory, **119**, pp. 184–197.
[15] Ballantyne, G. H., and Moll, F., 2003, "The Da Vinci Telerobotic Surgical System: The Virtual Operative Field and Telepresence Surgery," Surg. Clin., **83**(6), pp. 1293–1304.
[16] Shim, S., Ji, D., Lee, S., Choi, H., and Hong, J., 2020, "Compact Bone Surgery Robot With a High-Resolution and High-Rigidity Remote Center of Motion Mechanism," IEEE Trans. Biomed. Eng., **67**(9), pp. 2497–2506.
[17] Afshar, M., Carriere, J., Meyer, T., Sloboda, R., Husain, S., Usmani, N., and Tavakoli, M., 2020, "Optimal Design of A Novel Spherical Scissor Linkage Remote Center of Motion Mechanism for Medical Robotics," In 2020 IEEE/RSJ International Conference on Intelligent Robots and Systems (IROS), Las Vegas, NV, Oct. 24, 2020–Jan. 24, 2021, IEEE, pp. 6459–6465.
[18] Chen, G., Xun, Y., Chai, Y., Yao, S., Chen, C., and Wang, H., 2021, "Design and Validation of a Novel Planar 2R1T Remote Center-of-Motion Mechanism Composing of Dual-Triangular and Straight-Line Linkages," ASME J. Mech. Rob., pp. 1–11.
[19] He, Y., Zhang, P., Jin, H., Hu, Y., and Zhang, J., 2016, "Type Synthesis for Remote Center of Motion Mechanisms Based on Coupled Motion of Two Degrees-of-Freedom," ASME J. Mech. Des., **138**(12), p. 122301.
[20] Li, J., Zhang, G., Xing, Y., Liu, H., and Wang, S., 2014, "A Class of 2-Degree-of-Freedom Planar Remote Center-of-Motion Mechanisms Based on Virtual Parallelograms," ASME J. Mech. Rob., **6**(3), p. 031014.
[21] Huang, L., Yin, L., Liu, B., and Yang, Y., 2021, "Design and Error Evaluation of Planar 2DOF Remote Center of Motion Mechanisms With Cable Transmissions," ASME J. Mech. Des., **143**(1), p. 013301.
[22] Liu, S., Chen, B., Caro, S., Briot, S., Harewood, L., and Chen, C., 2016, "A Cable Linkage With Remote Centre of Motion," Mech. Mach. Theory, **105**, pp. 583–605.
[23] Ye, W., Zhang, B., and Li, Q., 2020, "Design of a 1R1T Planar Mechanism With Remote Center of Motion," Mech. Mach. Theory, **149**, p. 103845.
[24] Chen, C.-W., Chen, H.-C., Yang, H.-Y., Zeng, X.-Y., Wu, X.-H., and Chen, P.-C., 2022, "Intraocular Robotic Interventional System (IORBIS): Mechanical Design for Distally-Actuated Instrument Insertion and Automatic Tool Change," Mech. Mach. Theory, **167**, p. 104568.
[25] Suzuki, H., and Wood, R. J., 2020, "Origami-Inspired Miniature Manipulator for Teleoperated Microsurgery," Nat. Mach. Intell., **2**(8), pp. 437–446.
[26] Holton, L. L. H., 2000, Development of a Haptic Feedback Model for Computer Simulation of the Epidural Anesthesia Needle Insertion Procedure, The Ohio State University, Columbus, OH.
[27] Fati, N., Fitiwi, G., Aynalem, A., and Muche, A., 2021, "Depth of Spinal Needle Insertion and Its Associated Factors Among Patients Who Underwent Surgery Under Spinal Anesthesia," Transl. Res. Anat., **25**, p. 100143.